High-Speed 46-GHz 850 nm Photodetector with Inductive Peaking

Tianyu Long, Zhiyang Xie, Linze Li, Luyu Wang, Xinbo Zou, *Member, IEEE*, Haiming Ji, Juanjuan Lu, and Baile Chen, *Senior Member, IEEE*

Abstract—In this work, high-speed 850 nm GaAs/AlGaAs based dual-depletion-region photodetectors are demonstrated, which aim to meet the increasing need for bandwidth scaling and data rate in short-reach optical links. The devices exhibit the low dark current of ∼134.5 fA and responsivity of ∼0.44 A/W at 850 nm. The 3-dB bandwidth of 20 μm and 28 μm diameter devices with 50-ohm characteristic impedance transmission line were measured to be 29.72 GHz and 24.71 GHz respectively. While by incorporating inductive peaking via high characteristic impedance transmission line, the 20 μm and 28 μm diameter devices achieved maximum 3-dB bandwidth of 46.06 GHz and 36.09 GHz respectively. To the best of our knowledge, this 20 μm diameter device exhibits the highest 3-dB bandwidth among all the 850 nm photodetectors. This research showcases the potential of 850 nm dual-depletion-region photodetectors as promising solutions for high-speed short-reach optical communication systems, offering improved performance in terms of bandwidth and enabling the advancement of data transmission capabilities.

Index Terms—high-speed 850 nm photodetectors, dual-depletion-region photodetectors, inductive peaking.

I. INTRODUCTION

THE increasing demand for bandwidth scaling and data rates in modern data centers and high-performance computing (HPC) systems has created a significant need for short-range optical interconnects [1]–[4]. To meet this demand, there have been notable advancements in high-speed, low-threshold, and cost-effective 850 nm vertical cavity surface emitting laser (VCSEL) sources [5], as well as the development of 100 GHz electro-optic modulators operating at near-infrared (NIR) wavelengths around 0.8 μm [6]. These technologies are crucial for achieving high-speed interconnects in the next-generation data communication systems. In parallel, the receivers (Rx) in short-reach optical links, operating at 850 nm, require high-speed capabilities to handle the exponential growth in data traffic volume. Photodetectors operating at this wavelength play a vital role in these systems by converting optical signals into electrical signals, and their high-speed performance is crucial for ensuring efficient data transmission.

High-speed 850 nm photodetectors have been demonstrated using various materials such as Si [7]–[11], Ge [12], [13], GaAs/AlGaAs [14]–[18], InGaAs/InP [19], and InGaP/GaAs [20]. A Si p-i-n photodiode with a 3-dB bandwidth of approximately 19.1 GHz and quantum efficiency of 52% at 850 nm wavelength has been demonstrated [11]. The device utilizes periodic photon-trapping microstructures to enhance the weak absorption of Si at 850 nm. Ge/Si-based photodiodes have been investigated by G. Dehlinger et al., who achieved a 3-dB bandwidth of 29 GHz with a lateral p-i-n Ge-on-SOI detector [12]. However, Ge/Si photodiodes suffer from high dark currents due to lattice mismatch between Si and Ge. In contrast, direct bandgap semiconductors like GaAs and InGaAs offer advantages such as higher absorption coefficients and mobilities, making them more suitable for high-speed applications at 850 nm. In the GaAs/AlGaAs material system, F.-M. Kuo et al. demonstrated a zero-bias GaAs/AlGaAs photodiode with a 3-dB bandwidth of 13 GHz [16]. J. Shi et al. reported an InGaAs/InP photodiode with a 3-dB bandwidth of 21 GHz at a reverse bias of -3 V [19].

The design of carrier transport is critical for achieving high-speed operation. In pin-PDs, the transit-limited bandwidth is often limited by holes with lower mobility. D. Wu et al. reported on pin-photodiodes operating at 850 nm with diameters ranging from 15 μm to 25 μm, achieving the 3-dB bandwidths ranging from 24.8 GHz to 33.5 GHz [15]. On the other hand, the uni-traveling-carrier photodiode (UTC-PD) is a unique structure where only electrons with higher mobility transport in the depletion region [21], [22]. This design allows for the relaxation of holes in the p-type absorption layer, enhancing the high-speed performance. In our previous work [18], [23], we demonstrated a zero-bias modified uni-traveling-carrier photodiode (MUTC-PD), and the 20 μm device achieved a 3-dB bandwidth of 22.5 GHz.

China, and also with the University of Chinese Academy of Sciences, Beijing 100049, China (e-mail: longty2022@shanghaitech.edu.cn; xiezhy@shanghaitech.edu.cn).

Linze Li, Luyu Wang, Xinbo Zou, Juanjuan Lu and Baile Chen are with the School of Information Science and Technology, Shanghaitech University, Shanghai 201210, China (e-mail: lilz@shanghaitech.edu.cn; wangly4@shanghaitech.edu.cn; zouxb@shanghaitech.edu.cn; lujj2@shanghaitech.edu.cn; chenbl@shanghaitech.edu.cn).

Haiming Ji is with the University of Chinese Academy of Sciences, Beijing 100049, China (e-mail: jhm@semi.ac.cn).
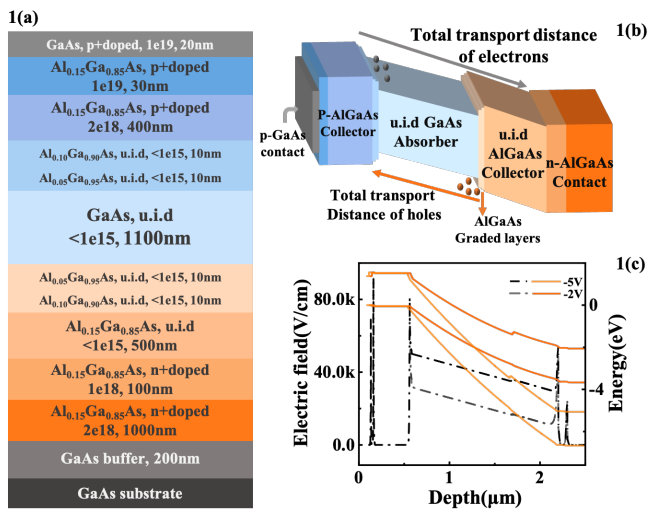
Fig. 1. Design and simulation of the device. (a) Epitaxial structure of the designed DDR-PD. (b) Schematic band diagram. (c)Stimulated energy band diagram (Solid line) and electric field of the device (Dash line).
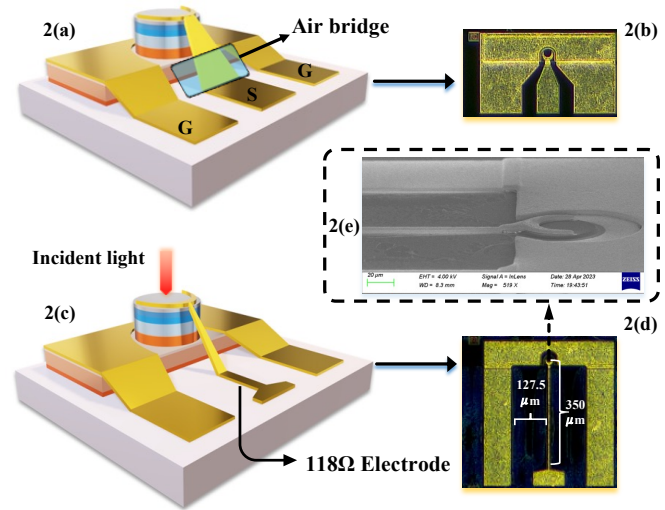

Fig. 2. Schematic diagram and fabricated device. (a) & (c) Schematic diagram of the device with different CPWs. (b) & (d) Corresponding fabricated devices. (e) SEM image of the fabricated crescent-shaped contact electrode.

In this work, we demonstrated the GaAs/AlGaAs based dual-depletion-region photodetectors (DDR-PDs). These DDR-PDs exhibit a faster photoresponse compared to pin-PDs with equivalent depletion thickness, primarily due to the smaller transition distance of holes compared to electrons in the dual-depletion region [24]. By optimizing the carrier transit time, the 20 μm and 28 μm diameter devices with 50-ohm characteristic impedance transmission line exhibited a 3-dB bandwidth of 29.72 GHz and 24.71 GHz respectively. Moreover, by implementing inductive peaking via a high characteristic impedance transmission line, we achieved even higher performance levels. Specifically, we obtained a maximum 3-dB bandwidth of 46.06 GHz for the 20 μm diameter device and 36.09 GHz for the 28 μm diameter device.

II. DESIGN AND FABRICATION OF DEVICE

The epitaxial structure of the designed photodetector, as depicted in Fig.1(a), was grown by a metal-organic chemical vapor deposition (MOCVD) system on a semi-insulating GaAs substrate. The n contact layer includes $n+$ 1000 nm and n 100 nm $Al_{0.15}Ga_{0.85}As$ layers. The dual-depletion-region is composed of un-intentionally doped 1100 nm GaAs and 500 nm $Al_{0.15}Ga_{0.85}As$ layers with two 10 nm graded AlGaAs layers employed to reduce the potential barrier at the heterojunction. Additionally, there is a $p+$ 400 nm layer and a p 30 nm layer of $Al_{0.15}Ga_{0.85}As$ acting as the p contact layer. Finally, a 20 nm p-type GaAs layer serves as the top contact layer.

Fig.1(b) illustrates the band diagram of the designed structure. Unlike the traditional pin-PD, the dual-depletion-region structure consists of a photo-transparent intrinsic $Al_{0.15}Ga_{0.85}As$ layer and an intrinsic GaAs absorption layer. This configuration results in a shorter transition distance for holes compared to electrons, allowing for balanced transit times. The thickness of $Al_{0.15}Ga_{0.85}As$ layer is considered carefully. Increasing the thickness of this layer initially leads to an improvement in bandwidth due to the shorter hole transport distance. However, further increasing the thickness will result in a decrease in

bandwidth, as the electron mobility in the $Al_{0.15}Ga_{0.85}As$ layer is comparatively lower than that in the GaAs layer. Simultaneously, the responsivity decreases as the GaAs absorber layer becomes thinner. Taking both bandwidth and responsivity into account, we set the thickness of the GaAs layer to 1100 nm and the $Al_{0.15}Ga_{0.85}As$ layer to 500 nm. Furthermore, the background doping concentration of the depletion region is controlled below 1×10^{15} cm^{-3}, allowing for complete depletion of the detector under low bias voltage and facilitating the quick drift of photogenerated carriers to the contact layers. The stimulated band structure and electric field distribution of the device are displayed in Fig.1(c). Notably, the dual-depletion-region can be fully depleted under a low reverse bias.

As illustrated in Fig.2, the epitaxial sample was processed into double-mesa structures. The fabrication process of the device is as follows: The first mesa was etched by induced coupled plasmas (ICP) dry etching process and stopped at the n-type $Al_{0.15}Ga_{0.85}As$ contact layer. The second mesa was formed using a phosphoric acid-based wet etch ($H_3PO_4 : H_2HO_3 : H_2O = 1:1:10$) process, terminating at the semi-insulating GaAs substrate to provide isolation between devices. Ti/Pt/Au and Ge/Au/Ni/Au metals were deposited on the p-type GaAs and n-type $Al_{0.15}Ga_{0.85}As$ as electrode contact layers respectively, using electron beam evaporation followed by a rapid thermal annealing process. To improve optical coupling efficiency, a crescent-shaped p-contact electrode was introduced (as shown in the scanning electron microscope (SEM) image in Fig.2(e)). In addition, a surface passivation process was utilized to reduce leakage current [25]. Subsequently, a silicon nitride (SiNx) thin film was deposited using plasma enhanced chemical vapor deposition (PECVD) as an anti-reflection (AR) coating. Finally, an air-bridge structure was used to connect the coplanar waveguide structure mentioned above.

To improve the 3-dB bandwidth of the photodetector, we introduced inductive peaking based on a high characteristic impedance transmission line. As depicted in Fig.2(c) and
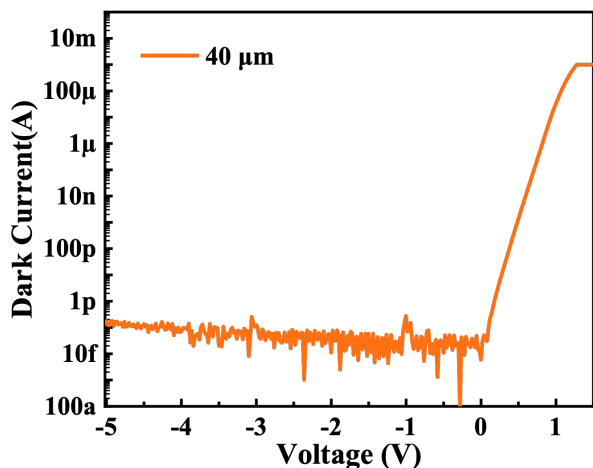
Fig. 3. Dark current (A) versus voltage (V) characteristic of the 40 µm diameter device at room temperature.

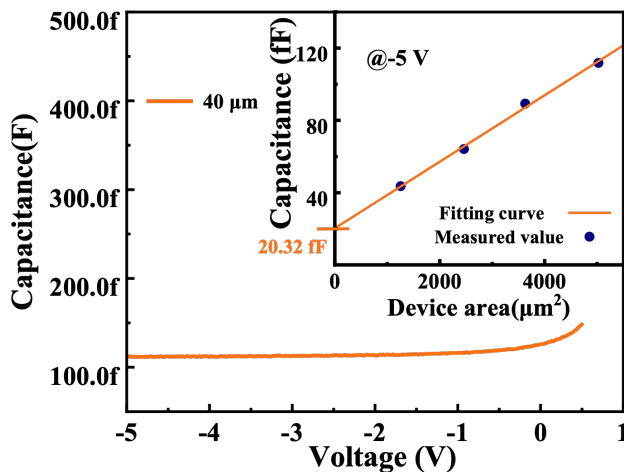

Fig. 4. Measured capacitance of the 40 µm diameter device. The insert shows the fitting curve at -5 v, indicating the parasitic capacitance of 20.32 fF

Fig.2(d), a 350 µm narrow-width waveguide electrode was introduced in the front section of the GSG (ground-signal-ground) electrode, positioned 127.5 µm away from the ground electrode. The characteristic impedance of the transmission line is calculated to be 118 ohms. For clarity, the devices with a 50-ohm characteristic impedance transmission line are referred to as 50-ohm transmission line photodiodes (50Ω-TL PD), while the devices with a high characteristic impedance transmission line are referred to as high impedance transmission line photodiodes (HI-TL PD).

III. DEVICE CHARACTERIZATIONS

A. Electrical Characteristics

Fig.3 presents the room-temperature dark current characteristics, the 40 µm diameter device exhibits extremely low dark current of 134.5 fA at a revise bias of -5 V. The corresponding dark current density is $1.07×10^{-8}$ A/cm2. Fig.4 shows the capacitance versus voltage (C-V) curves and capacitance versus device area curves at -5V of the 40 µm diameter device. The capacitance data maintains almost constant as the reverse bias increases, which indicates that the device is fully depleted under low reverse bias. By performing a linear fitting of the capacitance versus device area, the parasitic capacitance was determined as 20.32 fF.

B. Optical Characteristics

After the electrical characterization, we investigated the optical performance of the photodetectors. A system comprising a tungsten filament lamp and a grating spectrometer was used for quantum efficiency measurement. Since the spot size was relatively large, we compared the devices with a size of 500 µm to a commercially available silicon photodiode with calibrated responsivity. The quantum efficiency of the devices at different bias voltages (ranging from 0 V to -5 V) was measured, as shown in Fig.5. The 500 µm diameter devices exhibited a responsivity of approximately 0.44 A/W at 850 nm, corresponding to a quantum efficiency of about 65.6%. Notably, the responsivity of the photodetector exceeded 0.4 A/W in the

wavelength range of 770 nm to 850 nm. The insert in the figure presents the responsivity and coupling efficiency of devices with different diameters, which were measured using an 850 nm laser source.
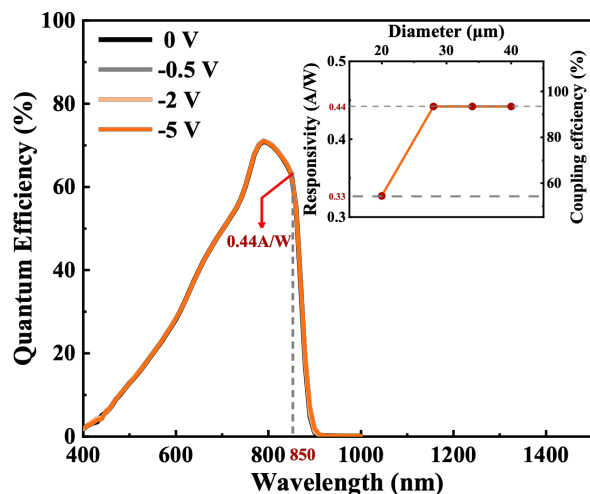

Fig. 5. Quantum efficiency spectrum at various bias voltages. The inset shows the responsivity and coupling efficiency of devices with different diameters

C. Bandwidth

The measurement setup for characterizing the frequency response of the devices at room temperature is shown in Fig.6. The 850 nm laser light, modulated by an 850 nm Mach-Zehnder modulator (MZM), was coupled to the device using a lensed fiber. The DC bias was provided through an external bias tee connected to a source meter, while the RF signal was captured by a Vector Network Analyzer (VNA) using an RF GSG probe. The frequency-dependent losses of the GSG and cables were accurately calibrated using the VNA. Finally, the measured data was calibrated with the S-parameter of the MZM, which was provided by the vendor.
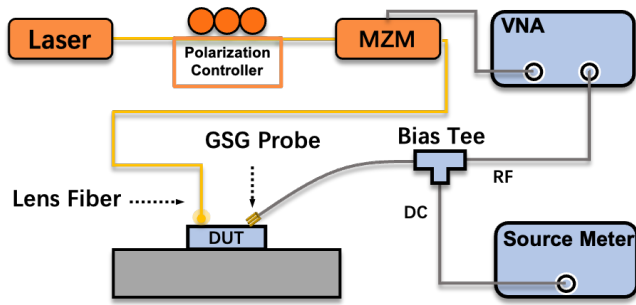
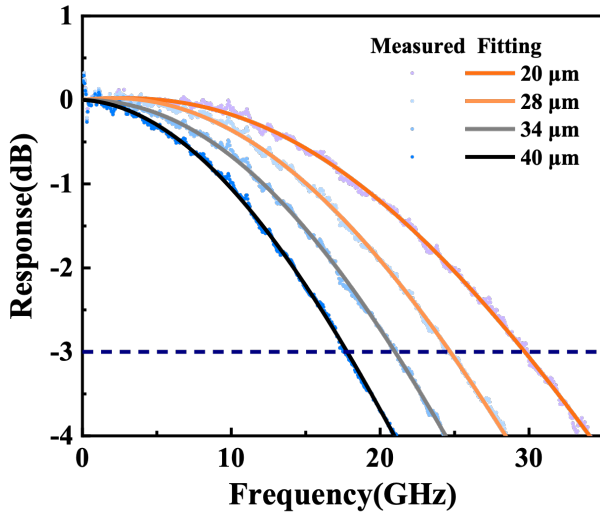Fig. 6. Schematic of frequency response measurement setup at 850 nm wavelength

Fig. 8. Equivalent circuit model of the DDR-PD for scattering parameters (S11) fitting

Fig. 7. Frequency response of the 50Ω-TL PD with different diameters under a reverse bias of -5 V

Fig. 9. The measured and fitting curve with 50 MHz-48 GHz frequency range of devices (50Ω-TL PD) under a reverse bias of -5 V.

1) 50Ω-TL PD

Figure 7 presents the frequency response of the 50Ω-TL PD with different diameters under a reverse bias of -5 V. The measured 3-dB bandwidths for the 20 μm, 28 μm, 34 μm, and 40 μm diameter devices were found to be 29.72 GHz, 24.71 GHz, 21 GHz, and 17.78 GHz, respectively. Theoretical analysis suggests that the 3-dB bandwidth of the photodiode is limited by the RC-limited and transit-time-limited bandwidth, which can be described by the following equation [18]:

$$\frac{1}{f_{3dB}{}^2} = \frac{1}{f_{RC}{}^2} + \frac{1}{f_{tr}{}^2} \tag{1}$$

where f_{3dB}, f_{RC}, and f_{tr} respectively represent the total 3-dB bandwidth, RC-limited bandwidth, and the transit-time-limited bandwidth. To investigate the impacts of f_{RC} and f_{tr} on f_{3dB}, we measured the scattering parameters (S11) of the devices using a Vector Network Analyzer (VNA). By combining the equivalent circuit model shown in Fig. 8 and the measured S11, we utilized the ADS software to fit the circuit parameters of the devices. The fitting process allowed us to determine the values of the junction resistance (R_j), which is typically very large at a reverse bias, the junction capacitance and parasitic capacitance (C_{PD}), and the series resistance (R_S), inductance (L_{cpw}), and capacitance (C_{cpw}) of the coplanar waveguide (CPW) pads.
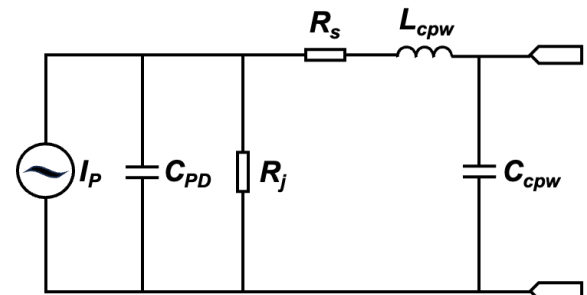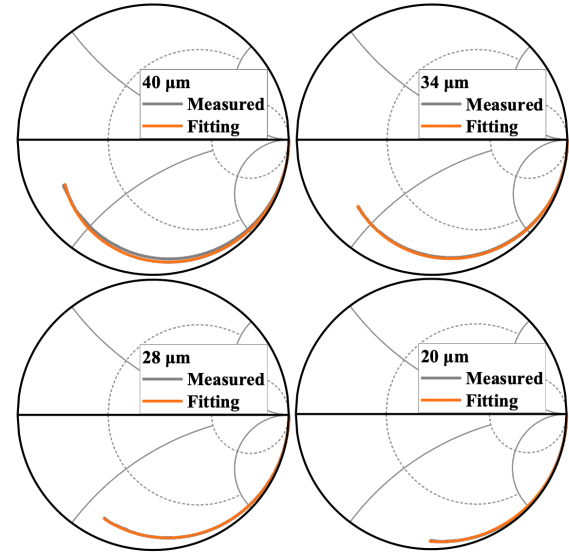
Figure 9 illustrates the measured and fitting (smooth line) curves of the devices under a reverse bias of -5 V. The extracted equivalent model parameters are provided in Table I, where R_j is not listed in the table (set to the order of 500 MΩ). Using these equivalent model parameters, the theoretical RC-limit frequency response can be calculated, as shown in Figure 10. It is observed that as the device diameter decreases, the junction capacitance also decreases, resulting in a higher RC-limit bandwidth.

Figure 11 displays the measured values of $1000/f_{3dB}{}^2$ plotted against the calculated values of $1000/f_{RC}{}^2$ for the 50Ω-TL PD. By applying Equation (1), the transit-time-limited bandwidth can be determined as 31 GHz from the intercept of the linear fit. Comparing this result to our previous work [18], an enhancement in the transit-time-limited bandwidth is observed at higher bias voltages, which can be attributed to the utilization of the dual-depletion structure in this study.

2) HI-TL PD

Fig.12 presents the frequency response of the HI-TL PD with different diameters under a reverse bias of -5 V. The 3-dB bandwidths of the 20 μm, 28 μm, 34 μm, and 40 μm diameter devices were measured to be 46.06 GHz, 36.09 GHz, 29.03 GHz, and 23.55 GHz, respectively. The equivalent circuit parameters obtained by fitting the S-parameters shown in the

This article has been accepted for publication in IEEE/OSA Journal of Lightwave Technology. This is the author's version which has not been fully edited and content may change prior to final publication. Citation information: DOI 10.1109/JLT.2023.3328899

> REPLACE THIS LINE WITH YOUR PAPER IDENTIFICATION NUMBER (DOUBLE-CLICK HERE TO EDIT) <   5

TABLE I
FITTING PARAMETERS

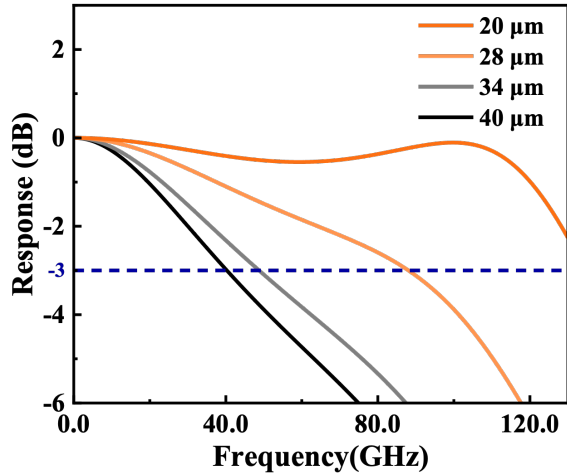| Device	Diameter (μm)	C_{PD} (fF)	R_S (Ω)	L_{cpw} (pH)	C_{cpw} (fF)
50Ω-TL PD	40	77.65	10.02	99.99	25.63
	34	65.16	11.72	99.44	24.54
	28	47.51	9.44	98.89	23.34
	20	31.1	7.14	98.24	23.85
HI-TL PD	40	124.48	16.23	313.85	23.66
	34	88.66	16.12	307.66	23.85
	28	69.92	12.6	307.59	24.70
	20	45.02	8.29	298.49	23.85

Fig. 10. Calculated RC-limited frequency response of the 50Ω-TL PD with different diameters using extracted circuit model parameters.
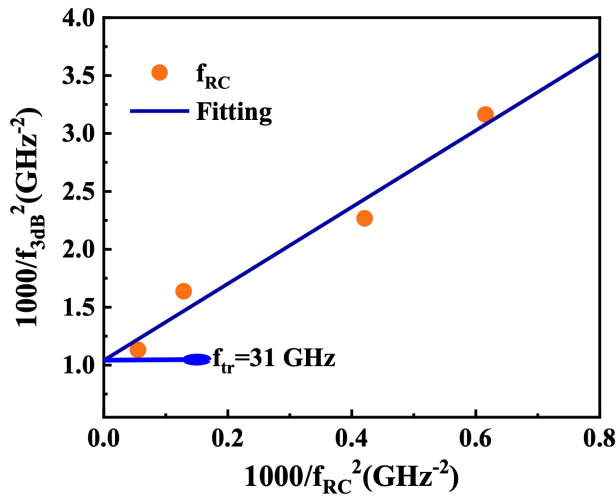

Fig. 11. Calculated f_{tr} using fitting curve with calculated ($1000/f_{3dB}^2$) versus measured ($1000/f_{RC}^2$)

Fig.13 are summarized in Table I. Notably, the HI-TL PD introduces a larger equivalent inductance compared to the 50Ω-TL PD.

In Fig.14, the RC-limited frequency response of devices with different diameters is shown. It can be observed that after introducing inductance, the device exhibits resonance, which means the transfer function exceed 0dB within a certain frequency range and the location of measured S11 valley
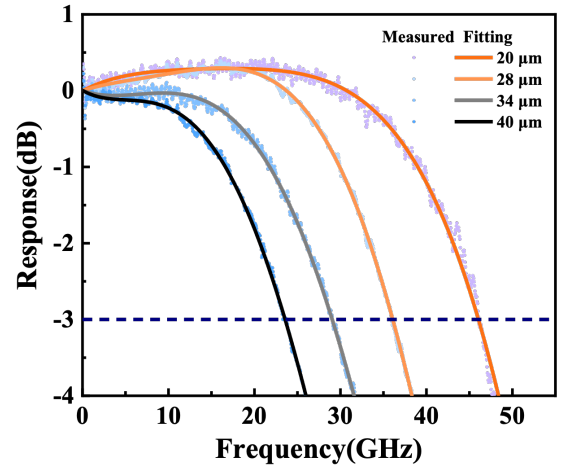
Fig. 12. Frequency response of the HI-TL PD with different diameters under a reverse bias of -5 V

Fig. 13. The measured and fitting curve with 50 MHz-48 GHz frequency range of devices (HI-TL PD) under a reverse bias of -5 V.

Fig. 14. Calculated RC-limited frequency response of the HI-TL PD using extracted circuit model parameters. The inset shows the location of S11 valley matching with the RLC resonant frequency ranges.

matches with the RLC resonant frequency ranges,

This article has been accepted for publication in IEEE/OSA Journal of Lightwave Technology. This is the author's version which has not been fully edited and content may change prior to final publication. Citation information: DOI 10.1109/JLT.2023.3328899
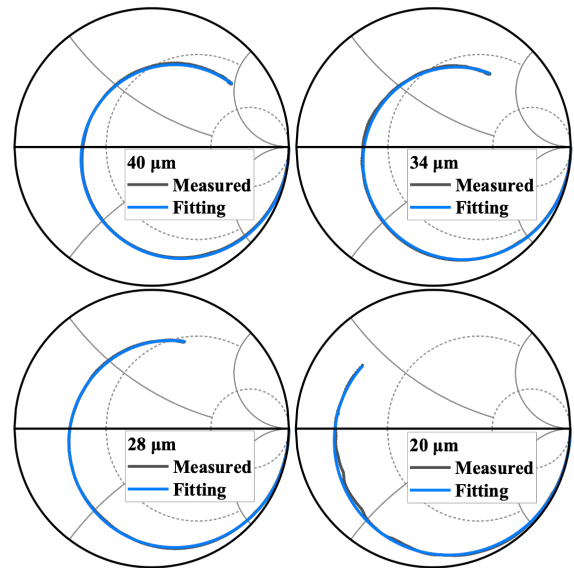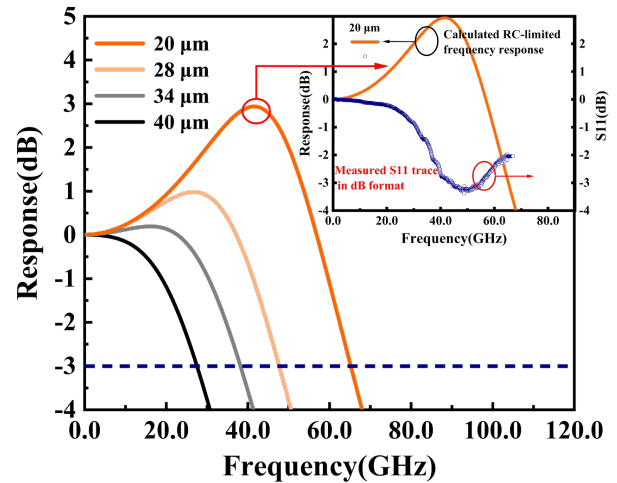
> REPLACE THIS LINE WITH YOUR PAPER IDENTIFICATION NUMBER (DOUBLE-CLICK HERE TO EDIT) <   6
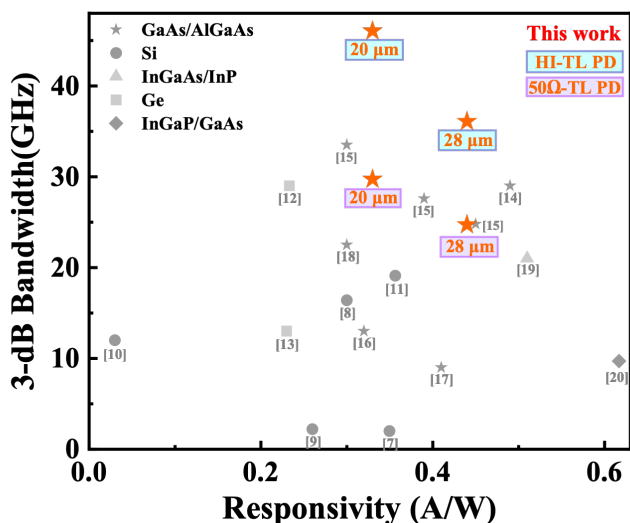
Fig. 15. The 3-dB bandwidth versus responsivity of the recently reported high-speed 850nm photodetectors

compensating for signal losses due to transit time limitation. The peaking effect contributes to a higher total 3-dB bandwidth of the photodetector.

Fig.15 presents a comparison of the 3-dB bandwidth versus responsivity among various high-speed 850 nm photodetectors reported in recent studies. It is noteworthy that our GaAs/AlGaAs-based dual-depletion-region photodetectors demonstrate superior bandwidth performance and high responsivity compared to other devices.

IV. Conclusion

In summary, we have successfully demonstrated high-speed 850 nm GaAs/AlGaAs dual-depletion-region photodetectors with excellent performance characteristics. These devices exhibit a low dark current and high responsivity, making them highly suitable for high-speed applications. Through careful control of carrier transit distance and the use of optimized RLC design, we achieved impressive 3-dB bandwidths. Under a reverse bias of -5 V, the 20 µm and 28 µm diameter devices with a 50-ohm characteristic impedance transmission line (50Ω-TL PD) achieved bandwidths of 29.72 GHz and 24.71 GHz, respectively. Additionally, by incorporating inductive peaking in the HI-TL PD devices, we further enhanced the bandwidth to 46.06 GHz and 36.09 GHz for the 20 µm and 28 µm diameter devices, respectively. These results represent the highest 3-dB bandwidth reported among all the 850 nm photodetectors. The demonstrated performance of our photodetectors underscores their potential for high-speed applications in optical communication systems.

References

[1] C. Xie et al., 'Real-Time Demonstration of Silicon-Photonics-Based QSFP-DD 400GBASE-DR4 Transceivers for Datacenter Applications', in 2020 Optical Fiber Communications Conference and Exhibition (OFC), Mar. 2020, pp. 1–3.

[2] D. Zhang et al., 'Consideration of Datacenter Optics for 400G and Beyond', Asia Communications and Photonics Conference, 2019.

[3] Q. Cheng, M. Glick, and K. Bergman, 'Optical interconnection networks for high-performance systems', in Optical Fiber Telecommunications VII, Elsevier, 2020, pp. 785–825. doi: 10.1016/B978-0-12-816502-7.00020-8.

[4] M. A. Taubenblatt, 'Optical Interconnects for large scale computing: How Do We Get Beyond the Cost & Power Wall?', in Optical Fiber Communication Conference (OFC) 2021, Washington, DC: Optica Publishing Group, 2021, p. Th4I.4. doi: 10.1364/OFC.2021.Th4I.4.

[5] H.-T. Cheng, Y.-C. Yang, T.-H. Liu, and C.-H. Wu, 'Recent Advances in 850 nm VCSELs for High-Speed Interconnects', Photonics, vol. 9, no. 2, p. 107, Feb. 2022, doi: 10.3390/photonics9020107.

[6] F. Valdez, V. Mere, and S. Mookherjea, '100 GHz bandwidth, 1 volt integrated electro-optic Mach–Zehnder modulator at near-IR wavelengths', Optica, vol. 10, no. 5, p. 578, May 2023, doi: 10.1364/OPTICA.484549.

[7] M. Yang et al., 'High speed silicon lateral trench detector on SOI substrate', in International Electron Devices Meeting. Technical Digest (Cat. No.01CH37224), Dec. 2001, p. 24.1.1-24.1.4. doi: 10.1109/IEDM.2001.979565.

[8] M. M. Pour Fard, C. Williams, G. Cowan, and O. Liboiron-Ladouceur, 'High-speed grating-assisted all-silicon photodetectors for 850 nm applications', Opt. Express, vol. 25, no. 5, p. 5107, Mar. 2017, doi: 10.1364/OE.25.005107.

[9] R. Swoboda and H. Zimmermann, '11Gb/s monolithically integrated silicon optical receiver for 850nm wavelength', in 2006 IEEE International Solid State Circuits Conference - Digest of Technical Papers, Feb. 2006, pp. 904–911. doi: 10.1109/ISSCC.2006.1696131.

[10] J.-S. Youn, M.-J. Lee, K.-Y. Park, and W.-Y. Choi, '10-Gb/s 850-nm CMOS OEIC Receiver With a Silicon Avalanche Photodetector', IEEE Journal of Quantum Electronics, vol. 48, no. 2, pp. 229–236, Feb. 2012, doi: 10.1109/JQE.2011.2170405.

[11] Y. Gao et al., 'Photon-trapping microstructures enable high-speed high-efficiency silicon photodiodes', Nature Photon, vol. 11, no. 5, pp. 301–308, May 2017, doi: 10.1038/nphoton.2017.37.

[12] G. Dehlinger, S. J. Koester, J. D. Schaub, J. O. Chu, Q. C. Ouyang, and A. Grill, 'High-Speed Germanium-on-SOI Lateral PIN Photodiodes', IEEE Photon. Technol. Lett., vol. 16, no. 11, pp. 2547–2549, Nov. 2004, doi: 10.1109/LPT.2004.835631.

[13] B. Ciftcioglu, J. Zhang, R. Sobolewski, and H. Wu, 'An 850-nm Normal-Incidence Germanium Metal–Semiconductor–Metal Photodetector With 13-GHz Bandwidth and 8-µA Dark Current', IEEE Photonics Technology Letters, vol. 22, no. 24, pp. 1850–1852, Dec. 2010, doi: 10.1109/LPT.2010.2089506.

[14] N. Dupuis et al., 'Exploring the limits of high-speed receivers for multimode VCSEL-based optical links', in Optical Fiber Communication Conference, San Francisco, California: OSA, 2014, p. M3G.5. doi: 10.1364/OFC.2014.M3G.5.

[15] D. Wu, Y.-T. Peng, X. Yu, and M. Feng, 'Process Optimization and Microwave Model of GaAs Photodiodes for 50 Gb/s Optical Links', IEEE Transactions on Semiconductor Manufacturing, vol. 33, no. 4, pp. 557–563, Nov. 2020, doi: 10.1109/TSM.2020.3016612.

[16] F.-M. Kuo, T.-C. Hsu, and J.-W. Shi, 'A GaAs/AlGaAs Based Uni-Traveling-Carrier Photodiode for 10Gbit/sec Optical Interconnect at 850nm Wavelength with Zero Electrical Power Consumption', in Optical Fiber Communication Conference and National Fiber Optic Engineers Conference, San Diego, California: OSA, 2009, p. OWX5. doi: 10.1364/OFC.2009.OWX5.

[17] J.-W. Shi, F.-M. Kuo, C.-S. Yang, S.-S. Lo, and C.-L. Pan, 'Dynamic Analysis of Cascaded Laser Power Converters for Simultaneous High-Speed Data Detection and Optical-to-Electrical DC Power Generation', IEEE Trans. Electron Devices, vol. 58, no. 7, pp. 2049–2056, Jul. 2011, doi: 10.1109/TED.2011.2136379.

[18] Z. Xie, Z. Zhou, L. Li, Z. Deng, H. Ji, and B. Chen, 'High-Speed 850 nm Photodetector for Zero-Bias Operation', IEEE Journal of Selected Topics in Quantum Electronics, vol. 28, no. 2: Optical Detectors, pp. 1–7, Mar. 2022, doi: 10.1109/JSTQE.2021.3095470.

[19] J.-W. Shi, K.-L. Chi, C.-Y. Li, and J.-M. Wun, 'Dynamic Analysis of High-Efficiency InP-Based Photodiode for 40 Gbit/s Optical Interconnect Across a Wide Optical Window (0.85 to 1.55 µm)', J. Lightwave Technol., vol. 33, no. 4, pp. 921–927, Feb. 2015, doi: 10.1109/JLT.2014.2364627.

[20] M.-C. Wu, Y.-H. Huang, and C.-L. Ho, 'High-Speed InGaP/GaAs p-i-n Photodiodes With Wide Spectral Range', IEEE Electron Device Letters, vol. 28, no. 9, pp. 797–799, Sep. 2007, doi: 10.1109/LED.2007.902609.

[21] Y. Chen, Z. Xie, J. Huang, Z. Deng, and B. Chen, 'High-speed uni-traveling carrier photodiode for 2 µm wavelength application', Optica, vol. 6, no. 7, p. 884, Jul. 2019, doi: 10.1364/OPTICA.6.000884.

This article has been accepted for publication in IEEE/OSA Journal of Lightwave Technology. This is the author's version which has not been fully edited and content may change prior to final publication. Citation information: DOI 10.1109/JLT.2023.3328899

> REPLACE THIS LINE WITH YOUR PAPER IDENTIFICATION NUMBER (DOUBLE-CLICK HERE TO EDIT) <   7

[22] J. Huang et al., 'High-Speed Mid-Wave Infrared Uni-Traveling Carrier Photodetector Based on InAs/InAsSb Type-II Superlattice', IEEE Electron Device Letters, vol. 43, no. 5, pp. 745–748, May 2022, doi: 10.1109/LED.2022.3163660.

[23] L. Wang et al., 'High-Speed Photodetector With Simultaneous Electrical Power Generation', J. Lightwave Technol., vol. 41, no. 2, pp. 662–670, Jan. 2023, doi: 10.1109/JLT.2022.3216839.

[24] F. J. Effenberger and A. M. Joshi, 'Ultrafast, dual-depletion region, InGaAs/InP p-i-n detector', Journal of Lightwave Technology, vol. 14, no. 8, pp. 1859–1864, Aug. 1996, doi: 10.1109/50.532024.

[25] H. Oigawa, J.-F. Fan, Y. Nannichi, H. Sugahara, and M. Oshima, 'Universal Passivation Effect of (NH 4) 2 S x Treatment on the Surface of III-V Compound Semiconductors', Jpn. J. Appl. Phys., vol. 30, no. 3A, p. L322, Mar. 1991, doi: 10.1143/JJAP.30.L322.